*J Nanostruct 15(3): 1291-1302, Summer 2025*

RESEARCH PAPER

# Annealing Effects on Physical and Sensing Characterization of Nanostructured MnO Thin Films

***Ahmed Nsaif Jasim***

*Department of Physics, College of Science, University of Diyala, Iraq*

## ARTICLE INFO

***Article History:***
*Received 11 March 2025*
*Accepted 15 June 2025*
*Published 01 July 2025*

***Keywords:***
*AFM*
*Annealing*
*Gas-sensing*
*MnO nanopaprticle*
*SEM*
*XRD*

## ABSTRACT

MnO thin films with different annealing temperatures were deposited via chemical spray pyrolysis. XRD analysis indicates that all films were polycrystalline with a dominant peak along the (111) plane. The average crystallite was increased via annealing temperature (400 to 500) °C. The dislocation density decreased from 50.33 to 42.18 nm when annealing temperature was raised from (400 to 500) °C. AFM was used to evaluate the morphology of the deposit films. As annealing temperature increased, the average particle size was measured to be between 77.6, 46.1, and 32.6 nm. SEM images show uniform spherical nano-grains, altering film morphology, which decreases with increasing temperature. The UV-Visible absorption spectra were utilized to obtain the optical parameters. Variations in film sensitivity to $NO_2$ at different annealing temperatures highlight intricate relationships between temperature, film responsiveness, and $NO_2$ concentration response. Oxidation induced by $NO_2$ in MnO film (400, 450, and 500) °C results in elevated resistance due to electron drift, correlating with sensitivity, with the highest resistance observed at 500 °C.

**How to cite this article**
*Jasim A. Annealing Effects on Physical and Sensing Characterization of Nanostructured MnO Thin Films. J Nanostruct, 2025; 15(3):1291-1302. DOI: 10.22052/JNS.2025.03.045*

## INTRODUCTION

Manganese oxide (MnO) is a transitional substance with remarkable physical and chemical properties [1]. Manganese oxide is a promising material for electrochemical lithium-ion batteries [2]. Through the easy insertion and extraction of lithium, high performance in electrochromic devices has also been enhanced [3]. Applications in optoelectronics have been sparked by it. It is utilized in magnetoelectronic devices [4], electrode materials [5, 6], electrochemical capacitors [7, 8], rechargeable batteries, and a variety of other applications. MnO exhibits various electrical and magnetic features, including metal-insulator transistors and massive magnetoresistance [9,10]. A transition metal oxide is manganese oxide. Band gaps for MnO range from 2.4 to 3.6 eV [11]. By various methods, ALD [12], PLD [13], EBD [14], thermal evaporation [15], plasma-assisted MBE [16], sol-gel [17], chemical spray pyrolysis [18], and CBD were some of the methods used to deposit manganese oxides thin films [5, 19]. Due to its ease of use, affordability, and capacity to increase the deposition area for commercial production, CBD is an excellent growth approach that has gained significant interest from the international scientific community [6]. This study describes how pure manganese via CBD produces MnO thin films. The physical characteristics of the films are established and explained in terms of those characteristics.

---

* *Corresponding Author Email: ahmedphy9@gmail.com*

## MATERIALS AND METHODS

CBD technology was utilized to create manganese oxide thin films with annealing variations on glass substrates. The glass slides are initially cleaned with a weak solution of hydrochloric acid (HCl, 1:5), which is followed by several rinses with distilled water and ethanol alcohol, as well as drying with special cleaning sheets. The following is the preparatory process: To achieve a concentration of 0.1 M, 1.70 g of copper (II) chloride ($MnCl_2.2H_2O$) is dissolved in 100 ml of deionized water. At room temperature, the resultant solution is a clear blue tint. The pH of the solution is then changed to 10 by adding ammonia ($NH_3$) at a concentration of 25–30 %. The substrates should be dipped into the solution once they boil at around 90°C. It takes about 7 minutes for anything to boil or 7 minutes for the temperature to rise from room temperature to 90 degrees Celsius. After boiling for 2.5 minutes, the substrates are removed from the bath and given a distilled water rinse. This study created three sets of samples to investigate how annealing affected films. After that, the films were each annealed for two hours at (400, 450, and 500) $^o$C in the air. Using the weighing approach, the sample's thickness was around 230 ± 25 nm. Shimadzu model: XRD 6000 diffractometer was employed to record the XRD pattern in the diffraction angle range of $0^o$ to $80^o$. The morphology was examined using AFM (AA 3000 Scanning Probe Microscope). The films underwent scanning electron microscopy (SEM) analysis using a JEOL-JSM-6360 model from Japan, operating at 20 kV. The VARIAN CARY MODEL 5000 spectrophotometer was used to acquire the absorption spectra of the MnO thin films. Gas-sensing experiments were conducted by placing the sample in a glass test chamber, coating it with MnO films, and conducting silver paste. Temperature variations were monitored using a sensitive thermocouple inside the sealed chamber. Changes in electrical resistance in response to $NO_2$ gas were measured with a Keithley 6514 DMM setup. Controlled amounts of $NO_2$ gas were delivered over the sample using a regulated flow meter (flow rate: 1 L per minute). All assessments of $NO_2$ gas sensitivity were carried out at an operational temperature of 125°C.

## RESULTS AND DISCUSSIONS

Multiple peaks in Fig. 1 indicate that the films are polycrystalline materials. Manganese oxide

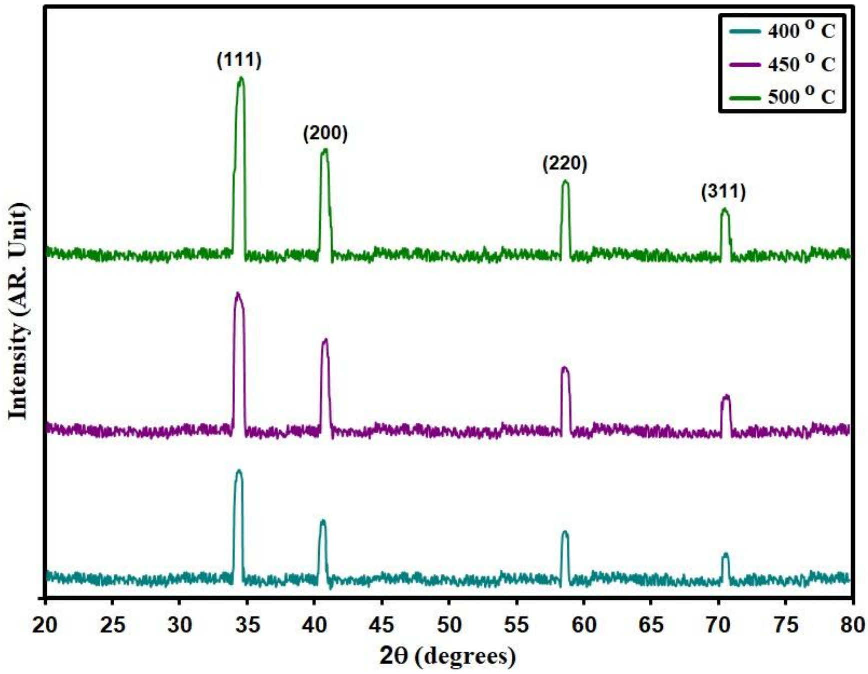

Fig. 1. XRD styles of grown films.

thin films exhibit distinct peaks at diffraction angles of 34.26°, 40.73°, 58.65°, and 70°. The comparison with JCPDS card No. (01-071-1177) suggests a preferred growth along the (111) orientation, with the peak at 2θ = 34.26° displaying significantly higher intensity [20, 21]. These findings imply a specific crystallographic orientation and preferred growth direction in the manganese oxide thin films.

The average grain size (*D*) for the dominated reflection (111) was calculated based on Scherrer's Eq. 1 and listed in Table 1 [22]:

$$D = \frac{K\lambda}{\beta\cos\theta} \tag{1}$$

K is the assumed form factor of 0.89, the incoming beam's wavelength (Cu $K_\alpha$ = 1.5406), β is FWHM, and θ is the Bragg angle. *D* was raised from 77.6 nm to 32.6 nm with an increase in

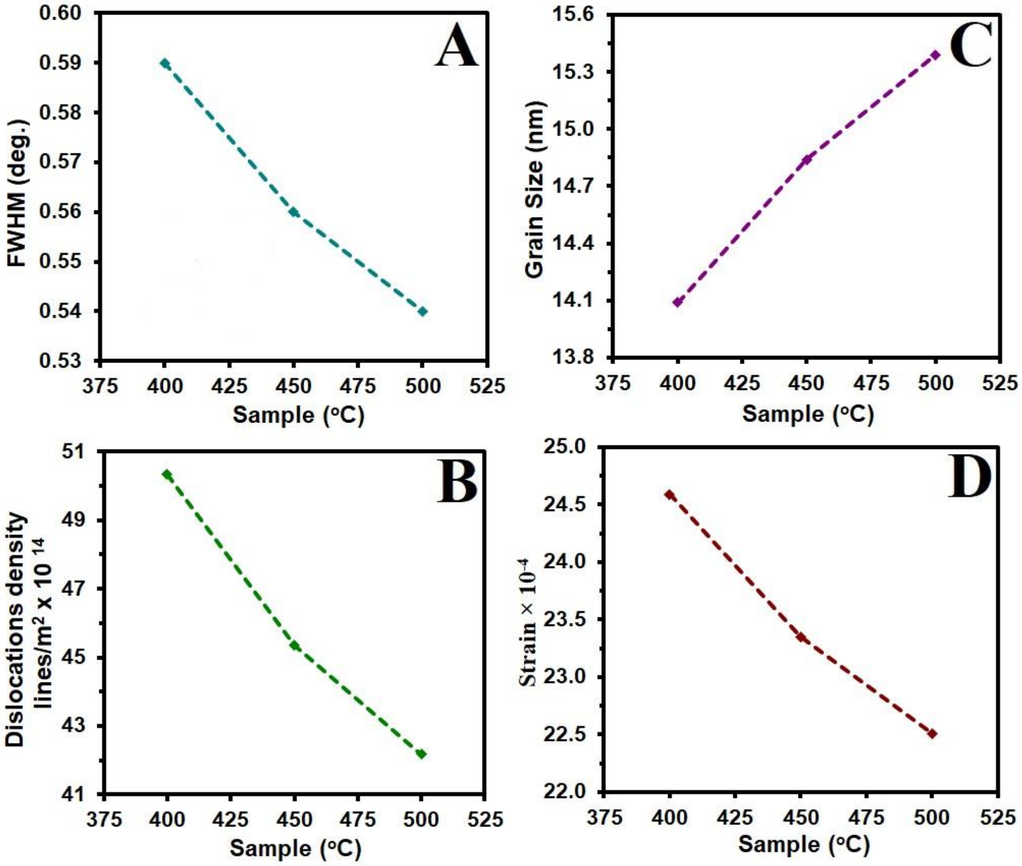

Fig. 2. FWHM (a) D (b) δ (c) ε (d) of the grown films.

Table 1. D, $E_g$ and $P_{st}$ of grown films.

| Specimen<br>°C | 2θ<br>(°) | (hkl)<br>Plane | FWHM<br>(°) | $E_g$<br>(eV) | *D*<br>(nm) | δ (× $10^{14}$)<br>(lines/m$^2$) | Strain<br>(× $10^{-4}$) |
|---|---|---|---|---|---|---|---|
| 400 | 34.26 | 111 | 0.59 | 3.42 | 14.09 | 50.33 | 24.59 |
| 450 | 34.21 | 111 | 0.56 | 3.37 | 14.84 | 75.35 | 23.35 |
| 500 | 34.19 | 111 | 0.54 | 3.30 | 15.39 | 42.18 | 22.51 |

annealing temperature ($T_{an}$) from 400 °C to 500 °C, respectively [23, 24], as shown in Table (1). The surface morphology is fine and regular with spherical nanoparticles (1).

The dislocation density (δ) for (111) was calculated using the formulae. [25]:

$$\delta = \frac{1}{D^2} \qquad (2)$$

The dislocation density is 50.33, 45.35 and

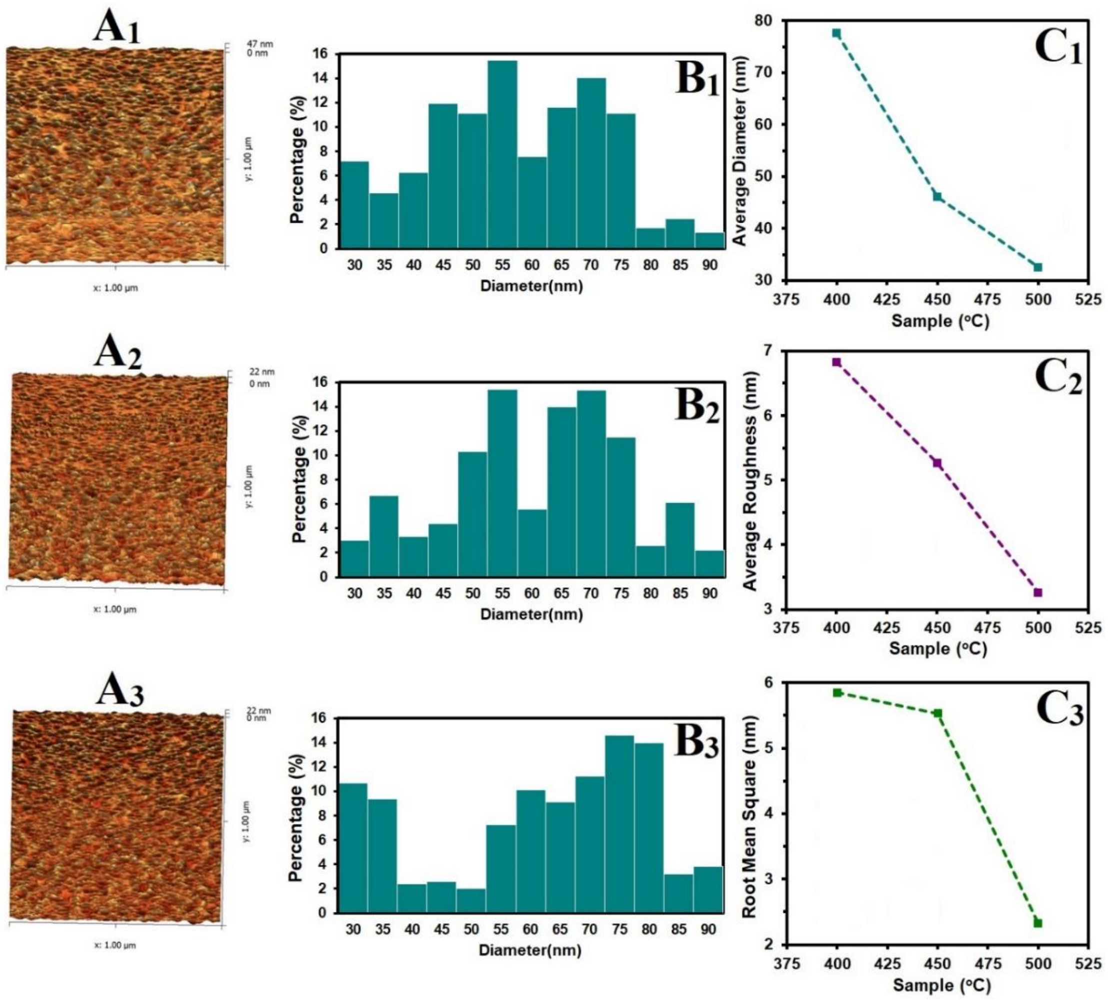

Fig. 3. AFM information.

Table 2. $P_{AFM}$ of the intended films.

| Specimen °C | $P_{av}$ nm | R (nm) | R. M. S. (nm) |
|---|---|---|---|
| 400 | 77.6 | 6.83 | 5.85 |
| 450 | 46.1 | 5.27 | 5.53 |
| 500 | 32.6 | 3.60 | 2.32 |

42.18 at $T_{an,}$ respectively.

The strain (Ɛ) for (111) was estimated using the Eq. 3 [26]:

$$\varepsilon = \frac{\beta\cos\theta}{4} \tag{3}$$

It was discovered that strain values as $T_{an}$ increased were 24.59, 23.35, and 22.51. Table 1 provides the computed structural parameters $P_{st}$. The inverse connection between grain size and other parameters is shown in Fig. 2, which shows the FWHM, *D*, dislocation density, and ε as functions of the produced films.

The three-dimensional AFM images in Fig. 3 ($A_1$, $A_2$, $A_3$) exhibit the properties of MnO thin films annealed at (400, 450, and 500) °C. The AFM images depict spherical-shaped grains that are uniformly distributed. Table 2 presents the Average Particle size ($P_{av}$) of MnO films, ranging from 77.6 to 32.6 nm, with root mean square (rms) values varying between 5.85 and 2.32 nm, and average surface roughness Ra ranging from 6.83 to 3.60 nm. A noteworthy observation is that as the annealing temperature increases, there is a consistent decrease in $P_{av}$, indicating a reduction in grain size. This trend is similarly observed for roughness. The AFM parameters ($P_{AFM}$) against MnO annealed at (400, 450, and 500) °C thin films are graphically represented in Fig. 3, while Table 2 provides a detailed list of PAFM values. These results suggest a correlation between the annealing temperature and the surface characteristics, influencing both particle size and roughness in MnO thin films [27, 28].

The SEM images illustrated in Fig. 4 show the synthesized films' morphological changes at different annealing temperatures. Initially, the surface is characterized by distinct, virtually flat islands. However, a transformation occurs as the annealing temperature increases, leading to a uniform surface coverage with spherical nano-grains. The decreasing size of these nano-grains with the gradual increase in annealing temperature suggests a correlation between the thermal treatment and the resultant nanostructure, highlighting the influence of annealing conditions on the film morphology [29, 30].

Fig. 4 shows the transmittance spectrum of thin MnO films that have been annealed at (400, 450, and 500) °C as a function of wavelength. It shows that the high transmittance region is at wavelengths between 450 and 900 nm for ultraviolet and visible light, while the low transmittance region is at wavelengths between 300 and 450 nm for visible light, which means that only about 10% of the transmittance occurs in the visible spectrum and 90% occurs in the ultraviolet spectrum [31, 32]. As the temperature annealing increases, the transmittance spectra of the films decrease, indicating satisfactory crystallinity of the achieved thicknesses. [33, 34].

The measured absorbance (A) of MnO thin films is related to transmittance (T) by [35]:

$$A = \log\left(\frac{1}{T}\right) = \left(\frac{I}{I_o}\right) \tag{4}$$

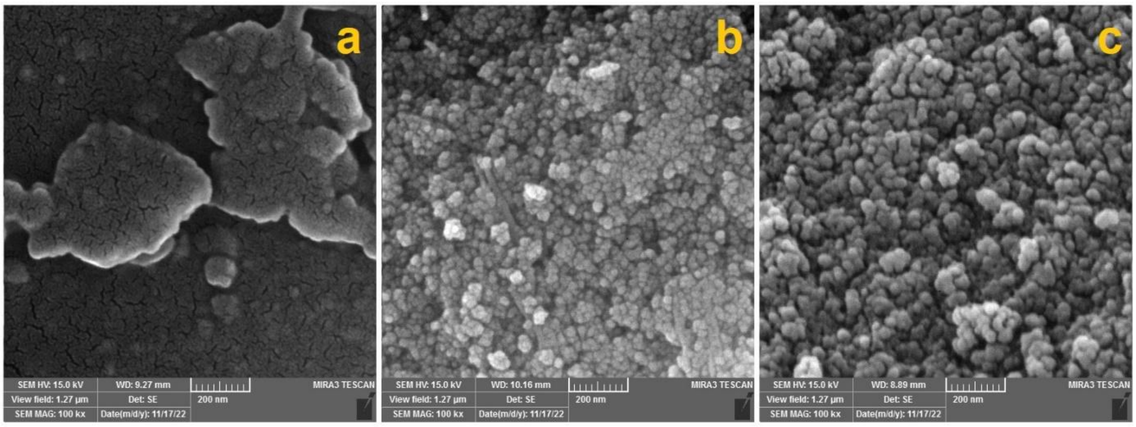

Fig. 4. SEM images of MnO: (a )400 °C, (b )450 °C , (c) 500 °C.

where (I) stands for incident light and (Io) for transmitted light. Fig. 6 plots the absorbance for the MnO thin films deposited in our study against the wavelength. A thorough examination of Fig. 6 reveals that the film is very absorbent in the visible region of the solar spectrum and that this absorbance progressively diminishes as the wavelength increases. The film annealed at 400 °C has weak infrared spectrum absorption [36, 37]. Fig. 6 demonstrates how absorbance rises as the annealing temperature rises.

The absorption coefficient (α) of MnO thin films

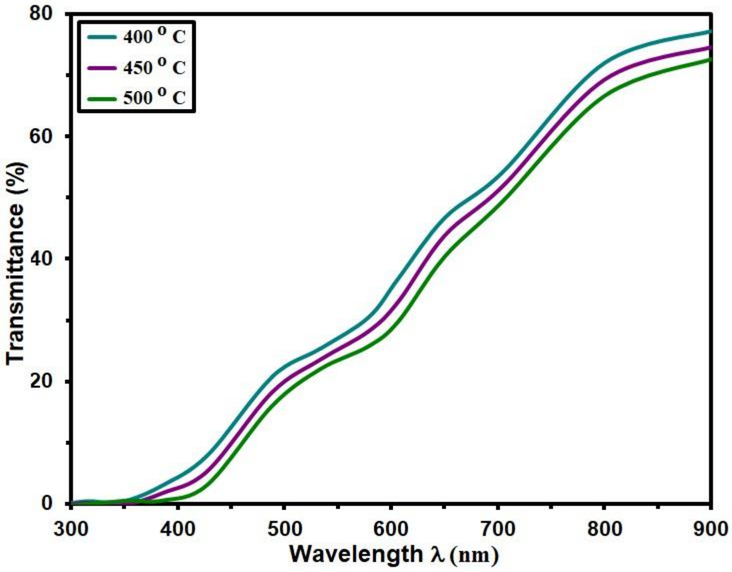

Fig. 5. T of the grown films.

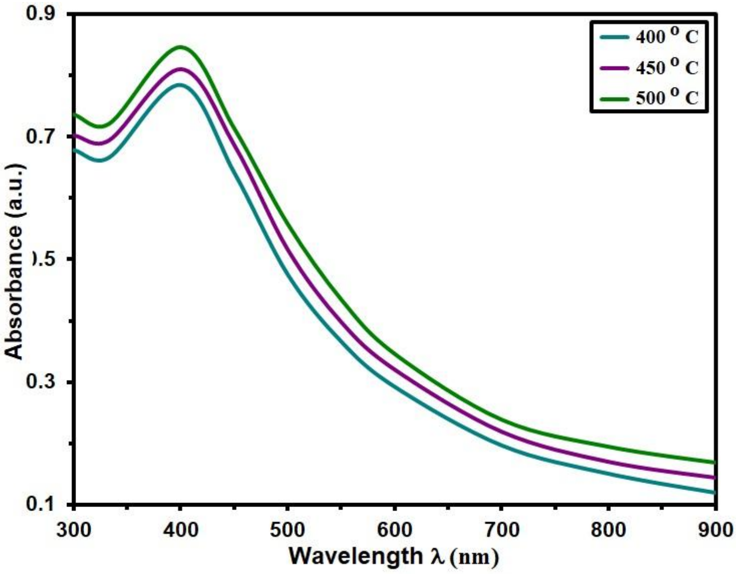

Fig. 6. A of the grown films.

was determined by using the Eq. 5 [38]:

$$\alpha = \ln(1/Td) \tag{5}$$

Where d is the film thickness. Fig. 7 illustrates the fluctuation of α with photon energy for various annealing temperatures (400, 450, and 500) °C (6). It should be noted that α of MnO thin films is on the order of $\alpha > (10^4)\ \mathrm{cm}^{-1}$, supporting the semiconductor's straight band gap nature [39]. Our findings support [40]. It is also evident that the films' absorption coefficient increases when

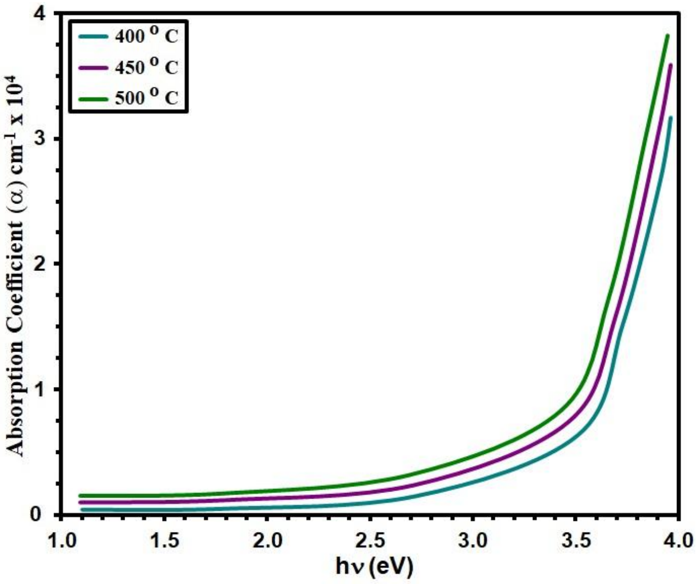

Fig. 7. α Vs hν of the prepared films.

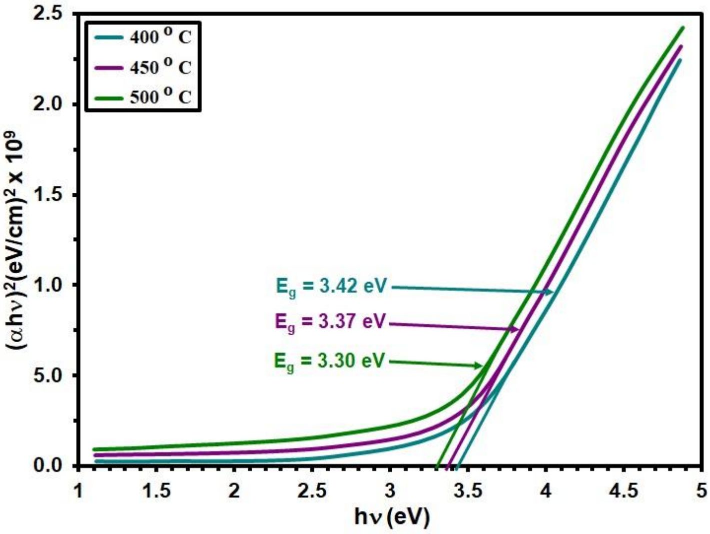

Fig. 8. $E_g$ of the grown film

$T_{an}$ rises. This is explained by the fact that as the annealing temperature rises, film absorbance rises, increasing the absorption coefficient.

Fig. 8 represents the relationship between $(\alpha h\upsilon)^2$ and (hv) according to Eq. 6 [41]:

$$(\alpha h\nu) = A\left(h\nu - E_g\right)^n \tag{6}$$

Where $E_g$ is the band gap, (hv) is the photon

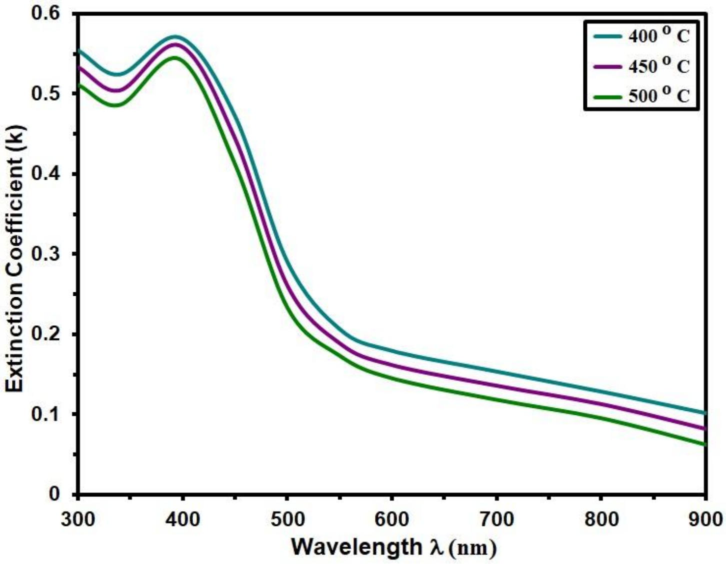

Fig. 9. k of the grown films.

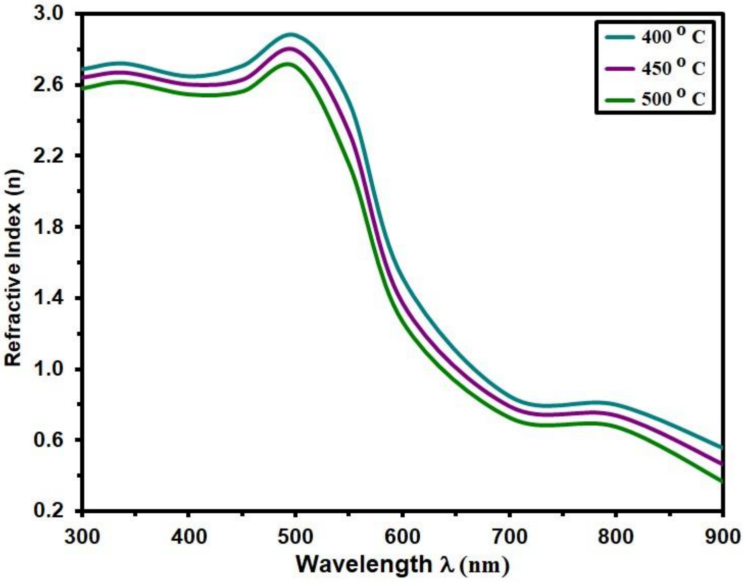

Fig. 10. n for grown films.

energy, A is the energy-independent constant, and the exponent n describes the characteristics of the band transitions. $E_g$ values were obtained by extending the linear component to the energy basis at n =0. The optical band gap was estimated and compared to the band gap energy derived from the optical transition occurring in the material and dropped from 3.42 to 3.30 eV, which are in

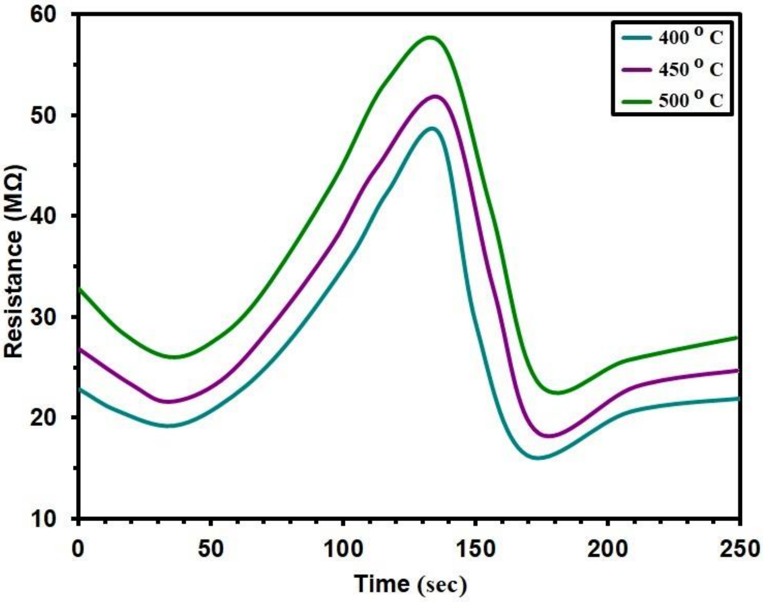

Fig. 11. Dynamic Resistance Change of MnO film annealed at (400, 450 and 500) °C.

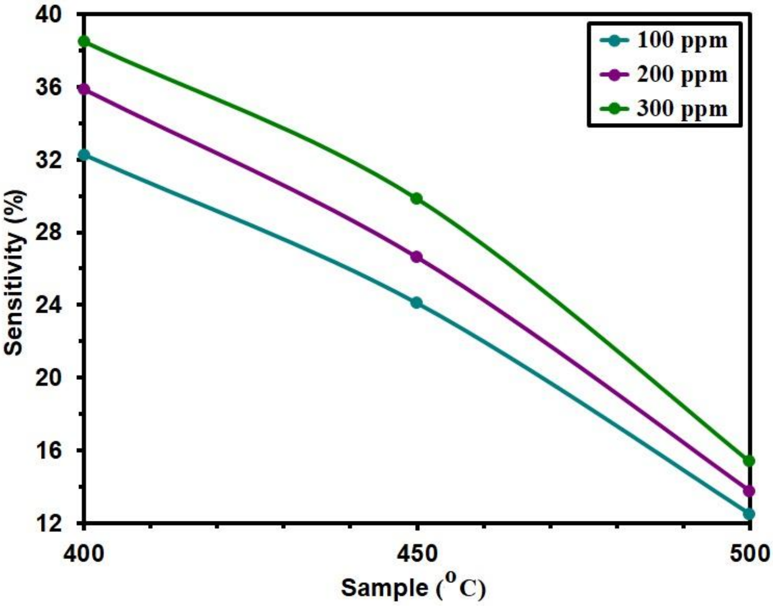

Fig. 12. Sensitivity of MnO annealed at (400, 450 and 500) °C.

excellent agreement with the reported values vis other methods. [42, 43].

Extinction coefficient (K) was evaluated according to Eq. 7 [44]:

$$k = \frac{\alpha\lambda}{4\pi} \tag{7}$$

Refractive index (n) was evaluated according to Eq. 8 [45]:

$$n = \left(\frac{1+R}{1-R}\right) + \sqrt{\frac{4R}{(1-R)^2} - k^2} \tag{8}$$

Figs. 9 and 10) show that these two factors—k and n—decreased as the annealing temperature increased, showing that the extinction coefficient was related to absorbance and influenced by the annealing temperature (8). At the same time, all films exposed in Fig.10 had refractive indices that ranged in value from 2.72 to 2.89 and were dependent on reflectivity (9). The composite is an absorbent material if its refractive index is increased to a high value. [46, 47].

In Fig. 11, the depicted relationship between resistance over time of MnO annealed at (400, 450, and 500) °C for 300 ppm of $NO_2$ and an operating temperature of 125 °C, which reveals the impact of $NO_2$ molecules, initiating an oxidation process on the surface. This process involves the liberation of bonded electrons to the surface by specific $O^{2+}$ ions, leading to the drifting of electrons back to the conduction band [48, 49]. Consequently, this electron drift increases resistance and the potential wall's reinforcement under these conditions [50, 51]. Notably, the MnO film annealed at 500 °C displays the highest resistance (R), demonstrating a direct correlation with film sensitivity and a robust resistance to gas flow [52].

The detection sensitivity, or sensor response, can be calculated using the Eq. 9 [53]:

$$\text{Sensitivity} = \frac{\Delta R}{R_g} = \left|\frac{R_g - R_a}{R_g}\right| \times 100\ \% \tag{9}$$

The sensitivity plots in Fig. 12 demonstrate how the sensitivity of the sensor changes with varying annealing temperatures (400, 450, and 500) °C after exposure to $NO_2$ gas. The observed reduction in sensitivity with increasing annealing temperature is attributed to the recombination process between the charge carriers of holes and electrons released from oxygen. This recombination process corresponds to the rising electrical resistance of the film [8]. In specific terms, for different annealing temperatures (400, 450, and 500) °C, the sensitivity dropped from 32.3% to 12.5% for 100 ppm, from 35.9% to 13.8% for 200 ppm, and from 38.5% to 15.4% for 300 ppm [54-56]. These trends suggest a complex interplay between annealing temperature, film sensitivity, and response to different concentrations of $NO_2$ gas.

## CONCLUSION

On a glass substrate, MnO thin films were created utilizing a straightforward and inexpensive chemical bath deposition process combined with annealing. They were thermally annealed to find out how thermal annealing affected the deposited films' structural, morphological, and optical features. The X-ray diffractogram analysis results show that MnO films have a cubic structure. The grain sizes increased as the annealing temperature rose from (400 to 500) °C, but strain dislocation and density values decreased as the temperature rose. AFM examinations showed a smooth surface morphology with root mean square roughness values decreasing from 5.85 nm to 2.32 nm for the annealed films. Due to annealing at 500°C, the average particle size exhibited the same trend. It reduced from 77.6 nm to 32.6 nm. From SEM images, Uniform spherical nano-grains emerge with annealing, reshaping film morphology. Nano-grain size diminishes as temperature rises. Calculations have been made for n and k and the absorbance, transmittance, and absorption coefficient. With a rise in annealing temperature, the optical constants fall. The annealed samples' permitted direct band gap shrank from 3.42 to 3.30 eV. $NO_2$-induced oxidation in MnO film (400, 450 and 500 °C) increases resistance due to electron drift, correlating with sensitivity and strong resistance at 500 °C. Sensitivity variation in $NO_2$-exposed films at different annealing temperatures, indicating a complex interplay between annealing temperature, film sensitivity, and response to varying concentrations of $NO_2$ gas.

## ACKNOWLEDGEMENTS

University of Diyala provided financial support for this project, for which the authors are grateful.

## CONFLICT OF INTEREST

The authors declare that there is no conflict of interests regarding the publication of this manuscript.

## REFERENCES

1. Kapteijn F, Vanlangeveld AD, Moulijn JA, Andreini A, Vuurman MA, Turek AM, et al. Alumina-Supported Manganese Oxide Catalysts. Journal of Catalysis. 1994;150(1):94-104.
2. Jamali M, Shariatmadar Tehrani F. Effect of synthesis route on the structural and morphological properties of $WO_3$ nanostructures. Mater Sci Semicond Process. 2020;107:104829.
3. Medina-Valtierra J, Ramírez-Ortiz J, Arroyo-Rojas VM, Ruiz F. Cyclohexane oxidation over Cu2O–CuO and CuO thin films deposited by CVD process on fiberglass. Applied Catalysis A: General. 2003;238(1):1-9.
4. Ahmadian H, Tehrani FS, Aliannezhadi M. Hydrothermal synthesis and characterization of $WO_3$ nanostructures: effects of capping agent and pH. Materials Research Express. 2019;6(10):105024.
5. Ma J, Chuah GK, Jaenicke S, Gopalakrishnan R, Tan KL. Catalysis by Manganese Oxide Monolayers Part 2: Zirconia Support. Berichte der Bunsengesellschaft für physikalische Chemie. 1996;100(5):585-593.
6. Astinchap B, Moradian R, Namdari T, Jurečka S, Ţălu Ş. Prepared σ-MnO2 thin films by chemical bath deposition methods and study of its optical and microstructure properties. Optical and Quantum Electronics. 2019;51(6).
7. Shaikh AA, Waikar MR, Sonkawade RG. Effect of different precursors on electrochemical properties of manganese oxide thin films prepared by SILAR method. Synthetic Metals. 2019;247:1-9.
8. Nilsen O, Fjellvåg H, Kjekshus A. Growth of manganese oxide thin films by atomic layer deposition. Thin Solid Films. 2003;444(1-2):44-51.
9. Bae SH, Lee SY, Jin BJ, Im S. Growth and characterization of ZnO thin films grown by pulsed laser deposition. Applied Surface Science. 2001;169-170:525-528.
10. Zhu H, Zhang J, Li C, Pan F, Wang T, Huang B. Cu2O thin films deposited by reactive direct current magnetron sputtering. Thin Solid Films. 2009;517(19):5700-5704.
11. Naeem R, Yahya R, Pandikumar A, Huang NM, Misran M, Arifin Z, et al. Photoelectrochemical properties of morphology controlled manganese, iron, nickel and copper oxides nanoball thin films deposited by electric field directed aerosol assisted chemical vapour deposition. Materials Today Communications. 2015;4:141-148.
12. Allah FK, Abé SY, Núñez CM, Khelil A, Cattin L, Morsli M, et al. Characterisation of porous doped ZnO thin films deposited by spray pyrolysis technique. Applied Surface Science. 2007;253(23):9241-9247.
13. Neubeck W, Ranno L, Hunt MB, Vettier C, Givord D. Epitaxial MnO thin films grown by pulsed laser deposition. Applied Surface Science. 1999;138-139:195-198.
14. Erlandsson O, Lindvall J, Toan NN, Hung NV, Bich VT, Dinh NN. Electrochromic properties of manganese oxide (MnOx) thin films made by electron beam deposition. Physica Status Solidi (a). 1993;139(2):451-457.
15. Dakhel AA. Correlated structural and electrical properties of thin manganese oxide films. Thin Solid Films. 2006;496(2):353-359.
16. Yan D, Yan P, Cheng S, Chen J, Zhuo R, Feng J, et al. Fabrication, In-Depth Characterization, and Formation Mechanism of Crystalline Porous Birnessite $MnO_2$ Film with Amorphous Bottom Layers by Hydrothermal Method. Crystal Growth &amp; Design. 2008;9(1):218-222.
17. Chen C-Y, Wang S-C, Tien Y-H, Tsai W-T, Lin C-K. Hybrid manganese oxide films for supercapacitor application prepared by sol–gel technique. Thin Solid Films. 2009;518(5):1557-1560.
18. Zhang X, Wu Z, Wang D, Wang D, Hou X. Erratum to "Improving the stability of organic light-emitting devices using a solution-processed hole-injecting layer" [Appl. Surf. Sci. 255 (2009) 7970–7973]. Applied Surface Science. 2010;256(11):3702-3703.
19. Xu HY, Xu SL, Li XD, Wang H, Yan H. Chemical bath deposition of hausmannite Mn3O4 thin films. Applied Surface Science. 2006;252(12):4091-4096.
20. Unuma H, Kanehama T, Yamamoto K, Watanabe K, Ogata T, Sugawara M. Journal of Materials Science. 2003;38(2):255-259.
21. Ching S, Hughes SM, Gray TP, Welch EJ. Manganese oxide thin films prepared by nonaqueous sol–gel processing: preferential formation of birnessite. Microporous Mesoporous Mater. 2004;76(1-3):41-49.
22. Thuraya Yarb S, Saif Khalel J, Ammar Ayesh H, Awatif Saber J. Preparation and Study Ag Nanoparticles via PLAL Technique: Influence of Different Number of Pulses. International Journal of Nanoelectronics and Materials (IJNeaM). 2024;17(1):45-51.
23. Rajabathar JR, Arunachalam P, Al-Lohedan HA, Thankappan R, Appaturi JN, Pulingam T, et al. Polymer surfactant (Triton-100) assisted low cost method for preparing silver and graphene oxide modified Bi-$MnO_x$ nanocomposite for enhanced sensor and anti-microbial health care applications. Journal of Sol-Gel Science and Technology. 2021;97(3):638-650.
24. Ramalingam RJ, Konikkara N, Al-Lohedan H, Al-dhayan DM, Kennedy LJ, Basha SKK, et al. Synthesis of MoS2 nanoparticle deposited graphene/mesoporous MnOx nanocomposite for high performance super capacitor application. International Journal of Hydrogen Energy. 2018;43(36):17121-17131.
25. Hameed SA, Bakr NA, Hassan AM, Jasim AN. Structural and optical properties of $Cu_2ZnSnS_4$ thin films fabricated by chemical spray pyrolysis. AIP Conference Proceedings: AIP Publishing; 2020. p. 020082.
26. Raymundo-Piñero E, Khomenko V, Frackowiak E, Béguin F. Performance of Manganese Oxide/CNTs Composites as Electrode Materials for Electrochemical Capacitors. Journal of The Electrochemical Society. 2005;152(1):A229.
27. Subramanian V, Zhu H, Wei B. Alcohol-assisted room temperature synthesis of different nanostructured manganese oxides and their pseudocapacitance properties in neutral electrolyte. Chemical Physics Letters. 2008;453(4-6):242-249.

28. Nilsen O, Fjellvåg H, Kjekshus A. Growth of calcium carbonate by the atomic layer chemical vapour deposition technique. Thin Solid Films. 2004;450(2):240-247.
29. Akita M. J Synth Org Chem Jpn. 2019;77(5):405-405.
30. Jothi Ramalingam R, Arunachalam P, Amer MS, AlOthman ZA, Alanazi AG, Al-Anazy MM, et al. Facile sonochemical synthesis of silver nanoparticle and graphene oxide deposition on bismuth doped manganese oxide nanotube composites for electro-catalytic sensor and oxygen reduction reaction (ORR) applications. Intermetallics. 2021;131:107101.
31. Rajabathar JR, Arunachalam P, Issa ZA, Ahmed M T. Synthesis and characterization of novel metal chalcogenide modified Ni-Co-MnO2 nanofibers rolled with graphene based visible light active catalyst for nitro phenol degradation. Optik. 2020;224:165538.
32. Ramalingam RJ, Al-Lohedan H, Tawfik AM, Periyasamy G, Muthumareeswaran MR. Synthesis and Characterization of $MoS_2$ –Grapene Oxide on Ni-Co-$MnO_2$ Nanofiber Like Binary Composite for Nickel Foam Based Flexible Electrode Fabrication. Chalcogenide Letters. 2020;17(8):423-428.
33. Li YW, Qiao Q, Zhang JZ, Hu ZG, Chu JH. Influence of post-annealing on structural, electrical and optical properties of manganese oxide thin films grown by atomic layer deposition. Thin Solid Films. 2015;574:115-119.
34. Ammundsen B, Desilvestro J, Groutso T, Hassell D, Metson JB, Regan E, et al. Formation and Structural Properties of Layered LiMnO[sub 2] Cathode Materials. Journal of The Electrochemical Society. 2000;147(11):4078.
35. Safardoust-Hojaghan H, Shakouri-Arani M, Salavati-Niasari M. A facile and reliable route to prepare of lead sulfate nanostructures in the presence of a new sulfur source. Journal of Materials Science: Materials in Electronics. 2014;26(3):1518-1524.
36. Isber S, Majdalani E, Tabbal M, Christidis T, Zahraman K, Nsouli B. Study of manganese oxide thin films grown by pulsed laser deposition. Thin Solid Films. 2009;517(5):1592-1595.
37. Chen CC, Yang C-Y, Lin C-K. Improved pseudo-capacitive performance of manganese oxide films synthesized by the facile sol–gel method with iron acetate addition. Ceram Int. 2013;39(7):7831-7838.
38. . NeuroQuantology. 2020;18(10).
39. Ren L, Wu S, Zhou W, Li S. Epitaxial growth of manganese oxide films on $MgAl_2O_4$ (001) substrates and the possible mechanism. Journal of Crystal Growth. 2014;389:55-59.
40. Chigane M, Ishikawa M, Izaki M. Preparation of Manganese Oxide Thin Films by Electrolysis/Chemical Deposition and Electrochromism. Journal of The Electrochemical Society. 2001;148(7):D96.
41. Abed ZA, Al Dulaimi AH, Shatti WA, Jasim AN, Khodair ZT, Khaleel SY. Structural and optical characterization of nanostructured undoped CuO and cobalt - doped CuO thin films. Journal of Ovonic Research. 2021;17(6):581-587.
42. Jothiramalingam R, Viswanathan B, Varadarajan TK. Zirconium Doped Tunnel Structure Manganese Oxide OMS-2 Catalysts. Eurasian Chemico-Technological Journal. 2004;6(2):117-122.
43. Rosid SJM, Toemen S, Wan Abu Bakar WA, Zamani AH, Wan Mokhtar WNA. Physicochemical characteristic of neodymium oxide-based catalyst for in-situ $CO_2$/$H_2$ methanation reaction. Journal of Saudi Chemical Society. 2019;23(3):284-293.
44. Jothiramalingam R, Viswanathan B, Varadarajan TK. Preparation, characterization and catalytic properties of cerium incorporated porous manganese oxide OMS-2 catalysts. Catal Commun. 2005;6(1):41-45.
45. Lo A-Y, Saravanan L, Tseng C-M, Wang F-K, Huang J-T. Effect of Composition Ratios on the Performance of Graphene/Carbon Nanotube/Manganese Oxide Composites toward Supercapacitor Applications. ACS Omega. 2019;5(1):578-587.
46. Kim KJ, Young Ran P. Sol–gel growth and structural and optical investigation of manganese-oxide thin films: structural transformation by Zn doping. Journal of Crystal Growth. 2004;270(1-2):162-167.
47. Achour A, Guerra A, Moulaï F, Islam M, Hadjersi T, Ahmad I, et al. $MnO_x$ thin film based electrodes: Role of surface point defects and structure towards extreme enhancement in specific capacitance. Materials Chemistry and Physics. 2020;242:122487.
48. Tsai SH, Duh JG. Microstructure and mechanical properties of CrAlN/SiN nanostructure multilayered coatings. Thin Solid Films. 2009;518(5):1480-1483.
49. Jiang J, Kucernak A. Electrochemical supercapacitor material based on manganese oxide: preparation and characterization. Electrochim Acta. 2002;47(15):2381-2386.
50. Pang S-C, Anderson MA, Chapman TW. Novel Electrode Materials for Thin-Film Ultracapacitors: Comparison of Electrochemical Properties of Sol-Gel-Derived and Electrodeposited Manganese Dioxide. Journal of The Electrochemical Society. 2000;147(2):444.
51. Toupin M, Brousse T, Bélanger D. Influence of Microstucture on the Charge Storage Properties of Chemically Synthesized Manganese Dioxide. Chem Mater. 2002;14(9):3946-3952.
52. Lee KH, Kim HJ, Choi JC, Park HL, Kim TW. Thermal annealing effects on the magnetic properties of (Ga1−xMnx)As thin films grown on GaAs (100) substrates. Journal of Crystal Growth. 2004;270(1-2):174-178.
53. Pang S-C, Anderson MA. Novel electrode materials for electrochemical capacitors: Part II. Material characterization of sol-gel-derived and electrodeposited manganese dioxide thin films. Journal of Materials Research. 2000;15(10):2096-2106.
54. Obodo RM, Nwanya AC, Arshad M, Iroegbu C, Ahmad I, Osuji RU, et al. Conjugated NiO-ZnO/GO nanocomposite powder for applications in supercapacitor electrodes material. International Journal of Energy Research. 2020;44(4):3192-3202.
55. Hameed SA, Kareem MM, Khodair ZT, Mohammed Saeed IM. The influence of deposition temperatures on the structural and optical properties for NiO nanostructured thin films prepared via spray pyrolysis technique. Chemical Data Collections. 2021;33:100677.
56. Khodair ZT, Alzubaidy MWM, Almohaidi AMS, Sultan AA, Al-Shimmary SMH, Albusultan SS. Synthesis of copper oxide nanoparticles (CuO-NPs) and its evaluation of antibacterial activity against P. aeruginosa biofilm gene's. AIP Conference Proceedings: AIP Publishing; 2019. p. 020006.